Indian Journal of Engineering & Materials Sciences
Vol. 30, December 2023, pp. 766-779
DOI: 10.56042/ijems.v30i6.2528

Parametric, Mechanical and Metallurgical Characterization of Dissimilar Friction Stir Welded AA2014-AA2219

Varthini Rajagopal[a], Dinesh Kumar Rajendran[b*], S. Muthukumaran[c]

[a]Department of Mechanical Engineering, Government College of Engineering Srirangam, Trichy 620 012, Inida

[b]Department of Mechanical Engineering, NIT Srinagar, Kashmir, 190 006, India

[c]Department of Metallurgical and Materials Engineering, NIT- Trichy, 620 015, India

Received: 9 June 2023; Accepted: 28 November 2023

In this study, Friction stir welding (FSW) is carried out on dissimilar aluminium alloys AA2219 and AA2014 using L16 orthogonal array based on Taguchi Mixed Factorial Design (TMFD) under four process variables: traverse speed, rotational speed, tilt angle and tool profile and the effects of FSW parameters on single and multiple responses (Tensile Strength, Yield Strength and Elongation) are analyzed using Response Surface Methodology (RSM) coupled with Augmented Epsilon Constraint Method (AUGMECON). Highest tensile strength and superior percentage elongation are attained at the parameter setting- 1400rpm Rotational Speed, 300mm/min Welding Speed, Tapered Threaded Pin tool profile and 3º Tilt Angle. Maximum yield strength is achieved under the parameter setting 800rpm Rotational Speed, 300mm/min Welding Speed, Tapered Threaded Pin tool and 3º Tilt Angle. A set of 20 optimal Pareto solutions providing a trade-off between the responses was generated. The rotation speed and tool tilt angle determined the trade-off between the extreme Pareto solutions. The microstructural analysis indicates finer grains in the bottom half compared to the top, with improved bonding between AA2219 and AA2014 in the nugget zone. Micro-hardness analysis reveals hardness similar to the parent material in the retreating side and poor hardness in the advancing side, where failures occur. SEM fractography shows a mixed ductile brittle fracture with elongated grains and uniform dispersion of intermetallics. Optimized parameters result in a disk-like planar morphology with a copper-rich GP zone, leading to improved strength and hardness. EDS mapping confirms presence of uniformly dispersed copper particles in the crater region that acts as a binder and resists void formation. XRD analysis further confirms the presence of Al_2Cu intermetallic phases.

Keywords: Al alloys, Characterization, Intermetallic, Dissimilar FSW, RSM-AUGMECON

1 Introduction

Age hardenable aluminium copper base 2xxx alloys of high strength with lesser weight are commonly used to overcome the challenges associated with structural application in aircraft and aerospace industries[1-2]. Al-Cu alloy, containing copper particles, has exceptional mechanical properties over the temperature span of -250°C to 260°C and therefore does not experience ductile to brittle transactions, making it suitable for holding liquid nitrogen and liquid oxygen of cryo engine fuel tanks[7]. Friction Stir Welding (FSW) has been considered an eminent welding process for producing high quality joints of heat treatable aluminium alloys compared to fusion welding. The technique of FSW was devised under the support of TWI, UK back in 1991[3]. Since then, it became the field of interest for both similar and dissimilar aluminium alloy welding for majority of the researchers[4]. In FSW, the heat generated due to the frictional contact surfaces of tool and workpiece results in plasticizing and interlocking of dissimilar/ similar material one over the other resulting in a superior bond formation[6]. Metal transfer in FSW occurs in two modes: first mode is through the tool shoulder and the other mode through the tool pin[8]. The emergence of an onion ring is adherent with the second mode where ring spacing is predominantly observed at lower rotation speed[9]. Tool tilt angle, followed by tool profile are found to have significant impact on increasing the weld strength[10]. In specific, screw pin tool profile resulted in weld joints with better mechanical property than normal pin[11-12]. The hardness of the weldment, with an improved strength due to lower grain size, observed at the friction stir zone was found closer to that of the parent materials[13-14]. A higher rotation speed of 16,000 rpm was found to have increased grain deformation in the retreating side than the advancing side[15]. The microstructure of stir zone exhibited dynamically recrystallized fine equiaxed grains and the grain size decreased as one

Table 1 — Chemical Composition of Base Material (Weight %)

Material	Cu	Mg	Zn	Mn	Si	Fe	Cr	Ti	Zr	Al
2219-T87	5.49	0.33	0.32	0.41	0.23	0.44	0.52	0.37	0.34	91.56
2014-T6	4.8	0.84	0.25	0.93	0.45	0.54	0.12	0.15	0.23	91.69

Table 2 — Mechanical Properties of Base Material

Material	Yield strength (MPa)	Ultimate Tensile Strength (MPa)	Elongation (%)	Vickers hardness (Hv)
2219-T87	389	463	12	145
2014-T6	320	440	14	140

moves downwards from the highest point of the stir zone[16]. In dissimilar welding, positioning of harder material on the advancing side is found to produce sound weld[17]. The precipitate evolution affects the hardness of every region and the coarsening of Al-Cu precipitate decreased the hardness in weld[18-19]. As AA 2219 and AA 2014 are high strength alloys with superior mechanical, metallurgical and corrosion properties, a lot of work have been carried out in similar welding of these two materials individually for numerous implementations. However, limited works[32-33] have reported on dissimilar welding of AA2219 and AA2014 which has a higher potential application in aerospace sector; especially in the counterpart connecting the cryogenic engine fuel tank and the inter-stage of space vehicles because of their low density and high strength and ductility when compared to those of AA2013 and AA2024 alloys. Since AA2219, though being a high strength alloy is highly resistant to stress corrosion cracking and AA2014 exhibits a high resistance to fatigue crack propagation[34], the dissimilar weldment of AA20219 and AA2014 might find a huge application in rocket tank manufacturing[33, 35].Hence, an attempt has been made in this research work to explore the weld possibility of AA2219 and AA2014 with improved mechanical and metallurgical properties. The main reason for weldment failure is observed due to coarsening or dissolving of precipitates. Hence, this research mainly focus on the dispersion of particles formed in the weld region rather than allowing it to get agglomerated in a particular region or dissolved in the stir zone by controlling and optimizing the process parameter[37,38].In this work, Taguchi Mixed Factorial Design (TMFD) is used for forming the design matrix and carrying out the experimental work[22] and the effects of FSW process parameters (rotational speed, transverse speed, tool profile and tilt angle) on the weld efficiency in terms of tensile strength, percentage elongation and yield strength are studied. Response Surface Methodology (RSM) was used to develop the mathematical models for the predicting the responses and branch and bound algorithm and augmented ε-constraint (AUGMECON) methods were used to optimize single and multi-responses.

Table 3 — Welding Levels and Parameters

Factors	Welding Parameters	Levels	Values
A	Rotational Speed (rpm)	4	800, 1000, 1200, 1400
B	Traverse Speed (mm/min)	4	150, 200, 250, 300
C	Tool Profile	2	TT*, CT*
D	Tilt angle (deg)	2	2°, 3°

1. TT: Tapered Threaded 2. CT: Cylindrical Threaded

2 Materials and Methods

Table 1 represents the chemical composition of the base materials and Table 2 depicts the mechanical properties observed in the base materials. In this analysis, Aluminium - Copper alloy 2219-T87 and 2014-T6 of 6mm thick rectangular plates with dimensions 100mm x 60mm were machined. AA2219 was positioned on the advancing end and AA2014 was kept in the retreating side[23] since material on advancing side would be subjected to more deformation (see Table 2).

The base materials' compositions were analysed using electron dispersion spectroscopy. The process parameters chosen were traverse speed, rotational speed, tool profile and tilt angle and were used for developing L16 orthogonal array with three parameters belonging to the two levels and two parameters belonging to the four levels as described in Table 3 & 4. Tool pin profiles of cylindrical Threaded (CT) and Tapered Threaded (TT) as depicted in Fig. 1. are used in this work. A 2-axis CNC Turning centre with D5 tool steel material is used to fabricte the tool. The machined tool exhibited a hardness of 45HRC. To improve the hardness, the machined tool was heat treated at an elevated temperature of 940°C with a constant heat rate of 220°C/hr and then soaked for 25 minutes, followed by oil-quenching. For tempering, the tool was again heated to 220°C at the same heating rate used in hardening and then soaked for 25 minutes and air cooled to increase the wear resistance. After heat

treatment, the hardness of the tool was found to be in the range of 55-65HRC. The tool was machined with flat and scrolled shoulder profile.

Biss 4 axis FSW Machine was used to carry out the dissimilar friction stir welding based on TMLD orthogonal array of L_{16}, as depicted in the Table 4, and the welded specimens were shown in Fig. 2.

Then welded specimens were incised using wire electrical discharge machine (WEDM) for tensile testing, hardness, and metallographic characterization. The tensile specimens were notched pertaining to the American Society for Testing of Materials (ASTM−E8M) standards into dog bone shape. Tensile tests conducted in this research was done using a Universal Testing Machine (UTM) that can be controlled electromechanically (Model: Tinius Olsen) with 1 mm/min strain rate. The Vickers Micro hardness Testing Machine (VMTM) (Model: Matsuzawa) has been employed for measuring hardness over the weld joint which has an indentation loading of 500gf for a holding time of 5s. Macro-structural and micro-structural analyses with grain size measurement were done using stereo and optical microscope (Model: Lyca) integrated with image analyzation software. Metallographic specimens were polished utilizing various grades of waterproof emery ranging from 200 – 2000 Grid size in the disc polisher. Consequent polishing was accomplished by alumina powder, followed by diamond polishing and fine cloth polishing with indigenous disk polishing setup. Keller's reagent was used as an etchant for micro-structural imaging and Kroll's reagent for macrostructure imaging in order to capture the nugget formation, metal flow phenomenon pattern from advancing to retreating sides and onion ring patterns. Scanning Electron Microscope (SEM) was employed for investigating the morphology corresponding to the

Table 4 — L_{16} Orthogonal Array by Taguchi Mixed Level Design

Trial No.	Rotational Speed(rpm)	Traverse Speed (mm/min)	Tool Profile	Tilt Angle (deg)
1	800	150	TT	2
2	800	200	TT	2
3	800	250	CT	3
4	800	300	CT	3
5	1000	150	CT	2
6	1000	200	CT	2
7	1000	250	TT	3
8	1000	300	TT	3
9	1200	150	TT	3
10	1200	200	TT	3
11	1200	250	CT	2
12	1200	300	CT	2
13	1400	150	CT	3
14	1400	200	CT	3
15	1400	250	TT	2
16	1400	300	TT	2

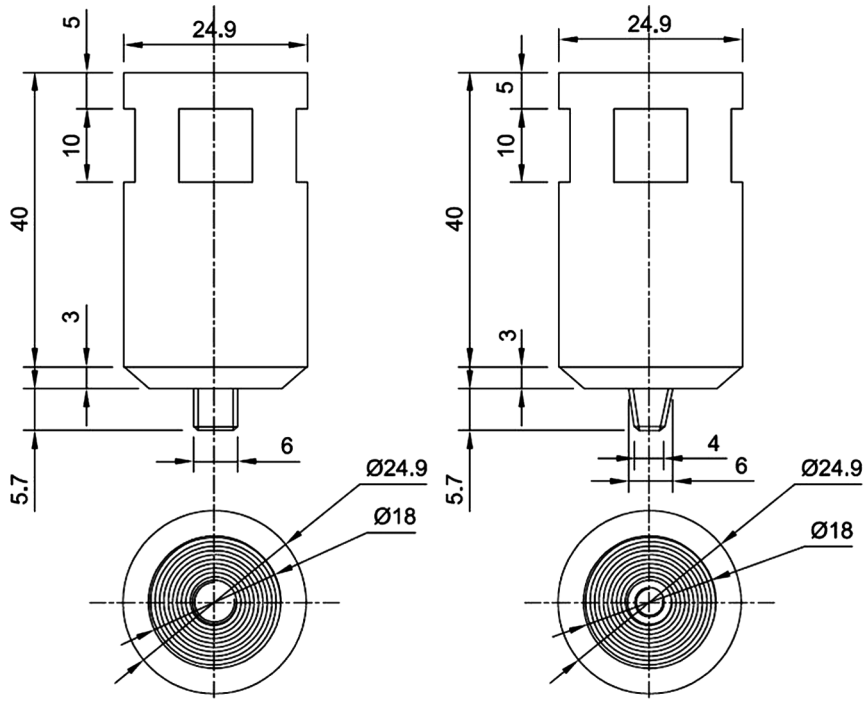

Fig. 1 — FSW Tool.

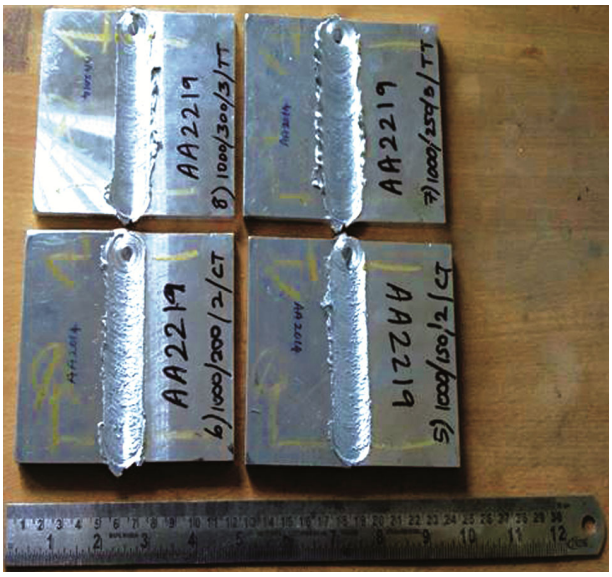

Fig. 2 — Welded Specimen.

Table 5 — Tensile Test Results

Trial No.	Tensile Strength (MPa)	Yield Strength (MPa)	Elongation (%)
1	242	197	2
2	283	195	5
3	338	202	7
4	343	211	8
5	230	202	2
6	302	206	4
7	329	208	7
8	344	209	7
9	341	202	7
10	316	196	6
11	254	203	3
12	270	211	3
13	337	188	8
14	328	197	7
15	347	203	8
16	351	213	8

surface where fracture occurred in the tensile tested specimens. Energy Dispersive Spectroscopy (EDS) was then utilized to study the above said tensile tested surface and investigate the precipitate's elemental composition. The composition of the precipitate, which controls the property of weld joint, was further confirmed with X-ray diffraction (XRD) analysis at a scanning rate of 0.02°/s.

3 Results and Discussions

The mechanical testing was carried out in UTM, and the tensile and yield strength values and the percentage elongation values pertaining to the 16 experimental trials are shown in Table 5.

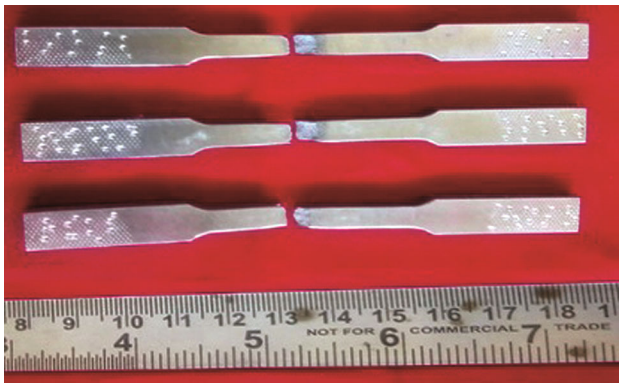

Fig. 3 — Fractured Tensile Samples.

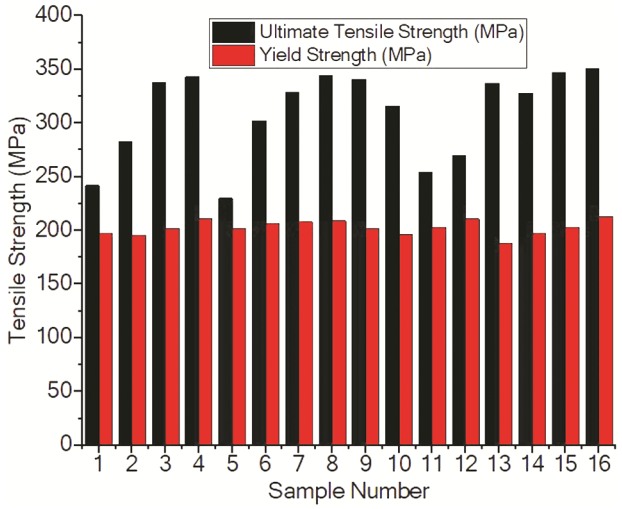

Fig. 4 — Mechanical Testing Result.

The fractured and mechanical testing results are shown in Fig. 3 and Fig. 4. Respectively.

The effects of FSW parameters on the responses are statistically analysed using Analysis of Variance (ANOVA). Response Surface Methodology (RSM) was used to develop the mathematical models for the responses and branch and bound algorithm and augmented ε-constraint (AUGMECON) method were used to optimize single and multi-responses.

3.1 Estimation of effect of FSW parameters on responses using ANOVA

ANOVA of yield strength, tensile strength, and percentage elongation were accomplished using Minitab 15 software. The percentages of contribution of FSW parameters under study to the weld strength were determined using general linear model. ANOVA of Ultimate Tensile Strength (UTS) was depicted in Table 6 and the result revealed the contribution of FSW parameters to UTS as: tool tilt angle contributed by 39.33%, rotational speed by 20.95%, traverse speed by 13.6%, and tool profile by 5.69%.The tool

tilt angle was found to have maximum effect on UTS and tool profile was perceived to have the least impact on UTS. From the main effect plot of FSW parameters on tensile strength (shown in Fig. 5), it can be observed that tensile strength increases incrementally with an increase in rotational speed from 800rpm to 1200rpm; beyond which a sharp rise in tensile strength with respect to rotation speed is noted. A rapid spike in tensile strength is also observed with an increase in traverse speed and tilting angle.Tapered Threaded tool profile exhibited better UTS compared to Cylindrical Threaded tool profile.

The main effect plot of FSW parameters on the yield strength was shown in Fig. 6 and ANOVA for yield strength was depicted in Table 7. Figure 6 shows that traverse speed and rotational speed have

Table 6 — ANOVA for Tensile Strength

Factors	DoF	Sum of Square	Mean Sum	F Value	Probability of Significance	% Contribution
Rotational Speed (mm/min)	3	5246.2	1748.7	2.39	0.154	20.95
Traverse Speed (mm/min)	3	3405.7	1135.2	1.55	0.284	13.6
Tool Profile	1	1425.1	1425.1	1.95	0.205	5.69
Tilt Angle	1	9850.6	9850.6	13.48	0.008	39.33
Error	7	5113.9	730.6			
Total	15	25041.4				

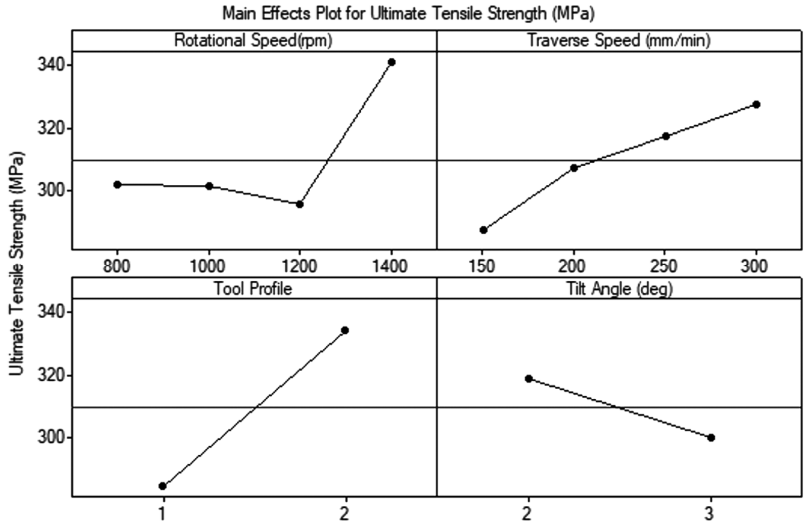

Fig. 5 — Main Effect Plot for Tensile Strength.

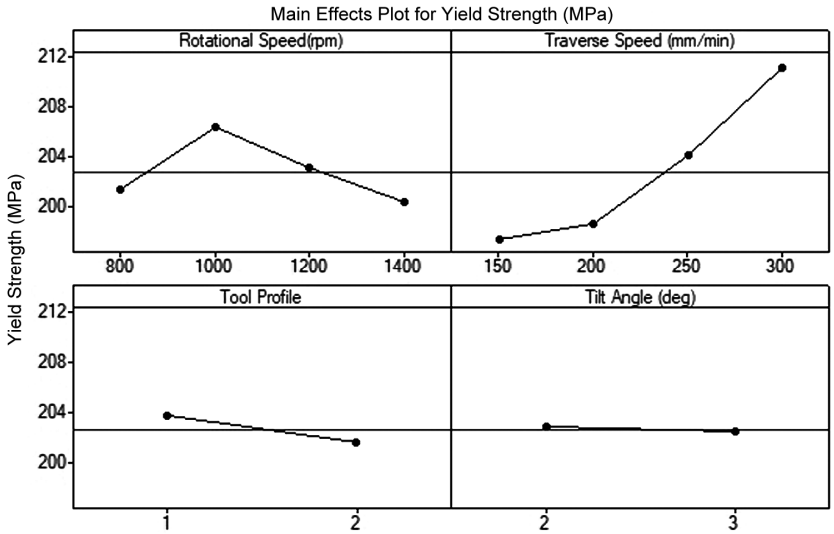

Fig. 6 — Main Effect Plot for Yield Strength.

significant effect on the yield strength and ANOVA quantified the contribution as 66.46% and 11.72 % respectively; whereas tilt and tool profile contributed 2.5% and 0.07% respectively. Maximized yield strength is given by a tool tilt angle of 2 degrees and a cylindrical threaded pin profile. These findings regarding yield strength of the weldment AA2014-AA2219 will be considerable aid to the aircraft manufacturing industries in which the elastic to plastic transition phase has a major impact on the design constraints of the material; since tolerance limit should be precise and should remain unchanged after fabrication.

ANOVA study for Elongation (%) is depicted in Table 8. The dependencies of elongation on FSW parameters were discovered as 40.33% due to tool tilt angle, 30% due to rotational speed, 10% due to traverse speed, and 5.3% due to the tool profile. Thus, the tool tilt angle has highest impact on elongation and the tool profile influences the elongation the least. The Fig.7 shows the main effect plot for elongation. From Fig. 7, it can be observed that % elongation incrementally decreases when rotational speed increases from 800rpm to 1200 rpm and increases sharply for a rotational speed beyond 1400 rpm. For a traverse speed of 150 mm/min to 300 mm/min, a significant rise in elongation is observed and the elongation elevates when tilt angle increases by a degree (i.e from 2 to 3 degree) and the Taper threaded tool resulted in higher elongation compared to that of

Table 7 — ANOVA for Yield Strength

Factors	DoF	Sum of Square	Mean Sum	F Value	Probability of Significance	% Contribution
Rotational Speed (mm/min)	3	83.19	27.73	1.43	0.313	11.72
Traverse Speed (mm/min)	3	471.69	157.23	8.10	0.011	66.48
Tool Profile	1	0.56	0.56	0.03	0.870	0.07
Tilt Angle	1	18.06	18.06	0.93	0.367	2.5
Error	7	135.94				
Total	15	709.44				

Table 8 — ANOVA for Elongation

Factors	DoF	Sum of Square	Mean Sum	F Value	Probability of Significance	% Contribution
Rotational Speed (mm/min)	3	22.500	7.500	4.88	0.039	30
Traverse Speed (mm/min)	3	7.500	2.500	1.63	0.268	10
Tool Profile	1	4.000	4.000	2.60	0.151	5.3
Tilt Angle	1	30.250	30.250	19.70	0.003	40.33
Error	6	10.750				
Total	15	75.000				

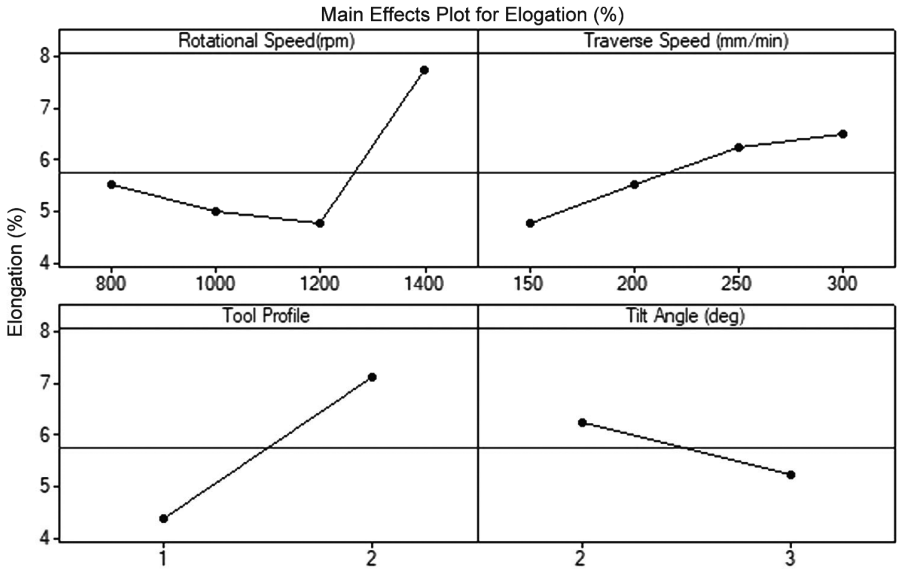

Fig. 7 — Main Effect Plot for % Elongation.

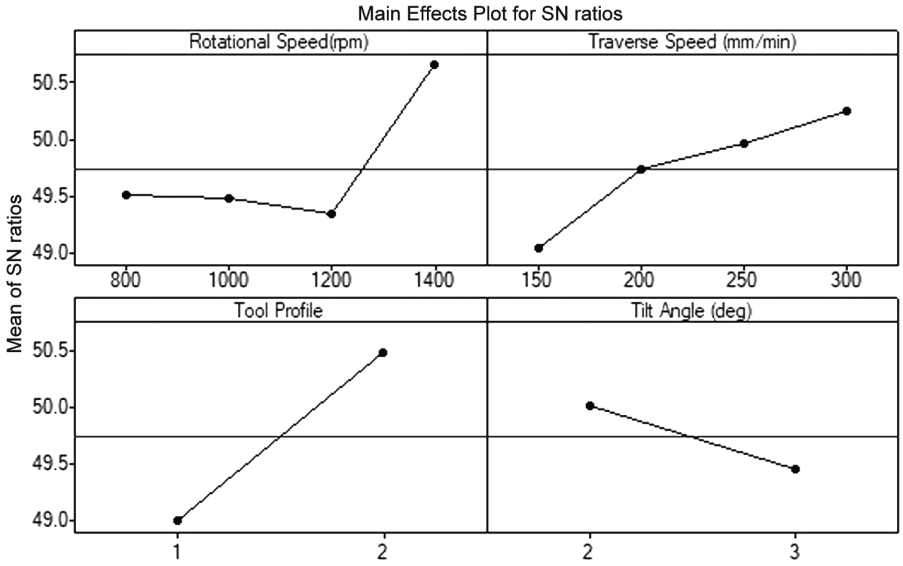

Fig. 8 — Main Effect Plot for SN Ratio.

the cylindrical thread profile.These findings regarding elongation property of AA2014-AA2219 will considerably aid aerospace industry, where complicated structures undergo forming operation after welding to get desired structure, as the elongation property has significant influence in establishing the formability of the welded product.

Higher values of the signal-to-noise (S/N) ratio identify parameter settings that minimize the effects of the noise factors. Higher the better S/N ratio is determined using equation (1):

$$\frac{S}{N} = -10log_{10}\left(\frac{1}{n}\sum_{i=1}^{m}\sum_{j=1}^{n}\frac{1}{z_{ij}}\right) \quad \ldots(1)$$

Where Z_{ij} represents the FSW input parametric value, and m and n denotes the number of input parameters and levels considered respectively. Fig. 8 shows the main effect plot for S/N ratio which exhibits a similar trend of UTS and elongation. Table 9 shows the larger the better S/N ratio corresponding to FSW input parameters and their levels.

From Table 9, it can be observed that higher S/N ratio is obtained at $A_4B_4C_1D_2$settings and the effect of FSW parameters on the noise is ranked as: Tilt angle, Rotational speed, Traverse speed and Tool profile.

3.2 Mathematical modelling using RSM and single response optimization using GAMS

In this section, for each response (Tensile strength, Yield Strength and Elongation) a mixed integer linear programming (MILP) mathematical model is developed in consideration with the FSW input parameters using Response surface methodology in Minitab. Further, the developed models are validated by estimating the regression coefficients using ANOVA. Then, the mathematical model is optimized in GAMS 23.5.1 on a 64-bit server with a 3.20 GHz Intel® Core(TM) i5-4570 CPU and 4GB of RAM using XPRESS solver which uses the approach of LP based branch and bound with cutting planes.

Table 9 — Response Table for S/N Ratios (Larger is better) corresponding to FSW input parameters and their levels

Level	Rotational Speed A	Traverse Speed B	Tool Profile C	Tilt Angle D
1	18.51	16.52	20.06	16.43
2	17.73	19.39	18.15	21.79
3	17.65	20.12		
4	22.58	20.41		
Delta	4.88	3.89	1.91	5.36
Rank	2	3	4	1

3.2.1 Mathematical modelling and optimization of Tensile Strength by RSM

The developed MILP model of Tensile Strength using RSM based on the experimental data in consideration with Rotational Speed (x_1), Traverse Speed (x_2), Tool Profile (x_3), and Tilt Angle (x_4)is given in eqn (2)- (7). The variable tool pin profile$x_3$is coded as '1' for TT profile and as '-1' for CT profile.

$$Maximise\ UTS = 66.45 + 0.0559x_1 + 0.2565x_2 + 9.4375x_3 + 49.6250x_4 \quad \ldots(2)$$

s.t.

$$800 \leq x_1 \leq 1400 \quad \ldots(3)$$

$$150 \leq x_2 \leq 300 \quad \ldots(4)$$

$$-1 \leq x_3 \leq 1 \quad \ldots(5)$$

$$2 \leq x_4 \leq 3 \quad \ldots(6)$$

$$x_3 \neq 0 \quad \ldots(7)$$

Where x_3 includes only positive and negative integers.

The adequacy of the developed MIP is testing statistically using ANOVA and the results are shown in Table 10.

Since the estimated p-value of the regression model is less than the F value (see Table 10) and the estimated co-efficient of determination (R^2) is greater than 80%, the developed model is highly significant and reliable respectively.

The developed MIP is then optimized using XPRESS solver coded in GAMS. The maximized UTS was found to be 379.972MPa under the optimal combination of 1400rpm Rotational Speed, 300mm/min Welding Speed, Tapered Threaded Pin tool profile and 3º Tilt Angle. This is in agreement with the ANOVA results of section 3.1.

3.2.2 Mathematical modelling and optimization of Yield Strength by RSM

Similarly, a MIP for yield strength is developed as shown in eqn (3) to (8)

$$Maximise\ YS = 190.400 - 0.003x_1 + 0.093x_2 + 0.188x_3 - 2.125x_4 \quad \ldots(8)$$

s.t.Eqn(3) to Eqn (7)

The adequacy of the developed MIP is tested statistically using ANOVA and the results are shown in Table 11.

Since the estimated p-value of the regression model is less than the F value (see Table 11) and the estimated co-efficient of determination (R^2) is greater than 80%, the developed model is highly significant and reliable respectively.

The developed MIP is then optimized using XPRESS solver coded in GAMS. The maximized YS was found to be 222.463MPa under the optimal combination of 800rpm Rotational Speed, 300mm/min Welding Speed, Tapered Threaded Pin tool and 3º Tilt Angle. This is also in agreement with the ANOVA results of section 3.1.

3.2.3 Mathematical modelling and optimization of Elongation by RSM

Similarly, a MIP for yield strength is developed as shown in Eqn (9) and Eqns (3) to (7)

$$Maximise\ Elongation = -7.4 + 0.00325x_1 + 0.01200x_2 + 0.5x_3 + 2.75x_4 \quad \ldots(9)$$

s.t. Eqn(3) to Eqn (7)

The adequacy of the developed MIP is testing statistically using ANOVA and the results are shown in Table 12.

Since the estimated p-value of the regression model is less than the F value (see Table 12) and the estimated co-efficient of determination (R^2) is greater than 80%, the developed model is highly significant and reliable respectively.

The developed MIP is then optimized using XPRESS solver coded in GAMS. The maximized elongation was found to be 9.5% under the optimal combination of 1400rpm Rotational Speed, 300 mm/min Welding Speed, Tapered Threaded Pin tool

Table 10 — ANOVA of the MIP model of UTS

Source	*DoF*	Seq SS	*Adj SS*	*Adj MS*	*F Value*	*P Value*
Regression	4	17062.8	17062.8	4265.71	5.88	0.009
Error	11	7978.6	7978.6	725.33		
Total	15	25041.4				

S = 26.9319 R^2 = 88.14% % R^2(adj) = 86.24%

Table 11 — ANOVA of the MIP model of YS

Source	*DoF*	Seq SS	*Adj SS*	*Adj MS*	*F Value*	*P Value*
Regression	4	463.550	463.550	115.887	5.18	0.014
Error	11	245.887	245.887	22.353		
Total	15	709.437				

S = 4.72794 R^2 = 85.34% R^2(adj) = 85.49%

Table 12 — ANOVA of the MIP model of Elongation

Source	*DoF*	Seq SS	*Adj SS*	*Adj MS*	*F Value*	*P Value*
Regression	4	49.9000	49.9000	12.4750	5.47	0.011
Error	11	25.1000	25.1000	2.2818		
Total	15	75.0000				

S = 1.51057 R^2 = 86.53% R^2(adj) = 84.36%

profile and 3º Tilt Angle. This is in agreement with the ANOVA results of section 3.1.

3.3 Multi Response Optimization using Augmented epsilon constraint method (AUGMECON)

To generate a set of Pareto optimal solutions, the multi-response mathematical model developed in Eqn (2)- (9) using RSM is subjected to an efficient AUGMECON algorithm. This posteriorior generation method, proposed by[17], is a development over the conventional epsilon constraint method, where each objective function is prioritized based on the decision maker's preference. AUGMECON is coded in GAMS 23.5.1 and solved using XPRESS solver[18].

$$Maximise\ UTS = 66.45 + 0.0559x_1 + 0.2565x_2 + 9.4375x_3 + 49.6250x_4 \quad \ldots(2)$$

$$Maximise\ YS = 190.400 - 0.003x_1 + 0.093x_2 + 0.188x_3 - 2.125x_4\ Eqn\ (8)$$

$$Maximise\ Elongation = -7.4 + 0.00325x_1 + 0.01200x_2 + 0.5x_3 + 2.75x_4 Eqn\ (9)$$

s.t.Eqn(3) to Eqn (7)

The maximized-maximized-maximized Pareto front of 20 solutions were generated and the corresponding optimal sets of input FSW parameters for 5 extreme Pareto solutions are shown in Fig. 9 and Table 13 respectively. The ideal solution point (IP) from the generated Pareto set is also plotted in Fig. 9. Depending on the decision maker's preference, a desired solution with a trade between UTS, YS and elongation can be selected from the Pareto set.

It can be observed from the Table 13 that the rotational speed and tilt angle decides the trade-off between UTS, YS and elongation. The UTS and Elongation take a higher value at the expense of yield strength when rotational speed and tilt angle are at higher level i.e., 1400rpm and 3 degrees respectively. The yield strength takes a higher value at the expense of UTS and Elongation when rotational speed and tilt angle are at lower level i.e., 800rpm and 2 degrees respectively. This is because at higher level of rotational speed and tilt angle, higher heat input is generated and the average grain size decreases and thereby maximizing the UTS and Elongation. Whereas at the lower levels of rotational speed and tilt angle, lower heat input is generated and the average grain size increases and hence yield strength increases[36].

Then validation experimental run was carried out for sample under parameter setting 1007.5rpm Rotational Speed, 300mm/min Welding Speed, Tapered Threaded Pin tool and 3º Tilt Angle and obtain tensile strength as 356MPa, yield strength as 209 MPa and elongation 8.3% which is a good approximate to the expected values.

3.4 Macrostructure and Microstructure Characterization

Figure 10 shows the macrostructural analysis carried on the Pareto solution (PS1) weld sample in order to differentiate the different zones in the weld region. The Fig. 10 clearly differentiates the First Mode of Metal Transfer (FMMT) formed under the influence of the tool shoulder, and the Second Mode of Metal Transfer (SMMT) by tool pin profile. Then other zones like Stir Zone (SZ), Thermo-Mechanically Affected Zone (TMAZ), Heat Affected Zone (HAZ), Base Metal (BM), and Onion Ring Pattern (ORP) are visibly observed and are labeled in

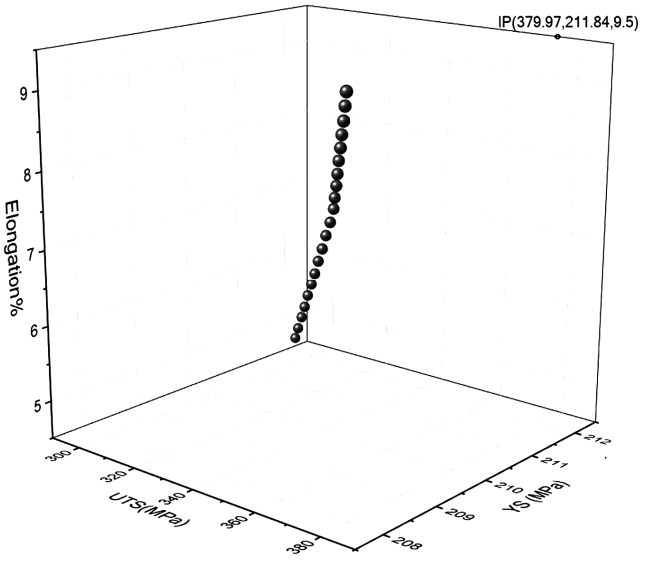

Fig.9 — Pareto Front of UTS, YS and Elongation.

Table 13 — Pareto solutions and their corresponding optimal levels

S.No	UTS(MPa)	YS(MPa)	Elongation	x_1	x_2	x_3	x_4
1	379.97	207.91	9.50	1400	300	1	3
2	358.032	209.091	8.224	1007.5	300	1	3
3	342.638	209.875	7.340	800	300	1	3
4	324.306	210.661	6.324	800	300	1	2.5
5	296.807	211.838	4.80	800	300	1	2

Fig. 10**.** The complete macro-structural examination was carried out at 4x magnification. The developement of the onion ring structure with a layered pattern formation and particle-rich alternate hard circles in the macrograpghy indicates the presence of additional strength enhancement phenomenon in AA 2219 and 2014 weldment[25-26].

The investigations of microstructures were performed using optical microscrope and the images were captured in the magnification of 400x with a marking scale of 25µm. Fig. 11 shows the images of the microstructure of the multi-response optimized weld specimen (PS1 16), captured at eight varying points.

On examination of the microstructure shown in Fig. 11, the transition between different zones caused by tool rotational deformation and the unaffected zone can be easily identified. Microstructure specimen 1 (refer Fig. 11) differentiates the distinct zones in the weld area as SZ, TMAZ, HAZ and the base materials i.e. 2219 and 2014 aluminium alloys**.** The transition between the FMMT and SMMT can be distinctly observed in microstructure specimen 2 (refer Fig. 11) at the advancing side. During the metal transfer, the first mode had elongated grains whereas the second mode had coarse grains. Microstructure specimen 3 (refer Fig. 11) is captured at the surface point where tool pin separates from shoulder. In this region,

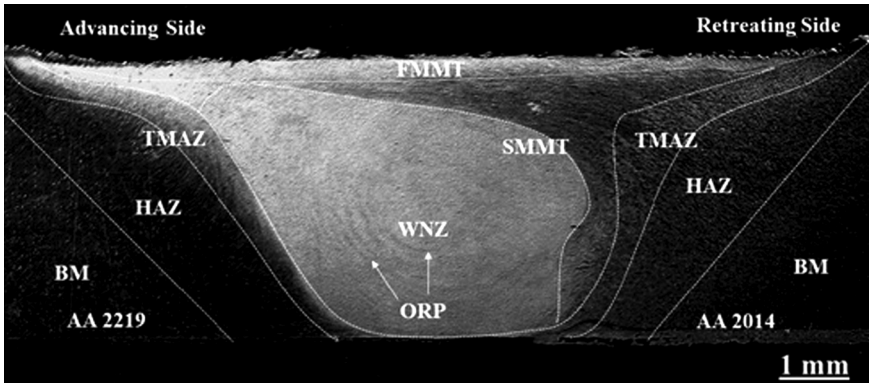

Fig. 10 — Macrostructure of AA2219-AA2014 weld.

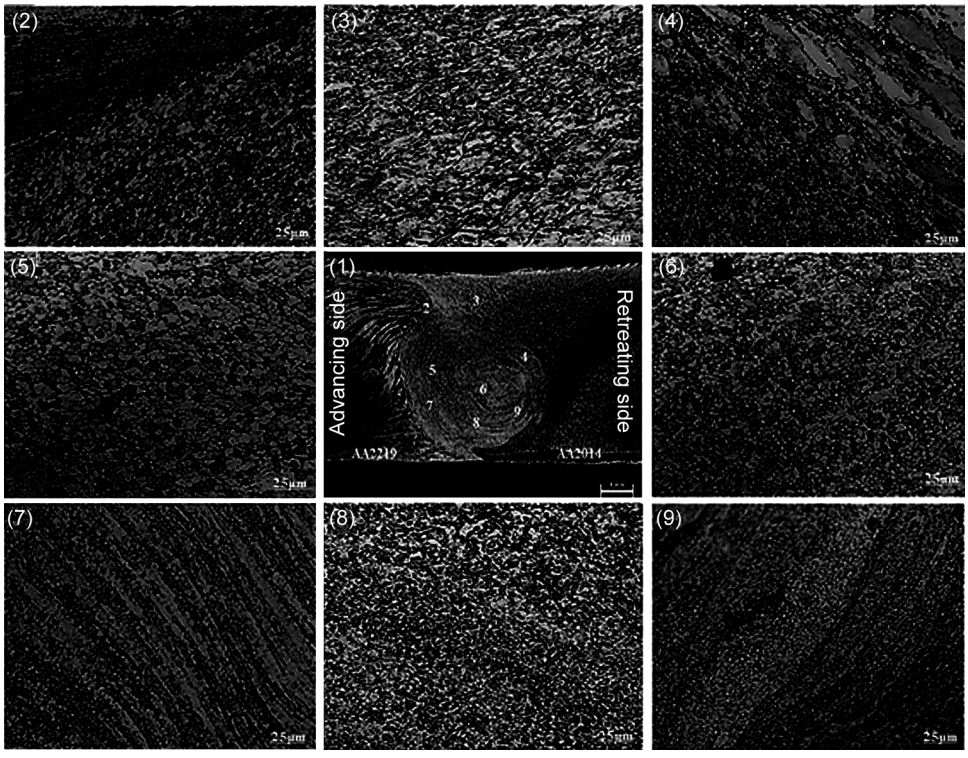

Fig. 11 — Microstructure of welded sample.

coaxial grain development is observed during the stirring process. Microstructure specimen 4 (refer Fig. 11), captured at the retreating side interface of SZ and TMAZ, indicates the presence of loosely packed elongated and coarser grains. Microstructure specimen 5 (refer Fig. 11), is captured at the advancing side of the SZ which has little larger equiaxed grains. Microstructure specimen 6 (refer Fig. 11) shows the equiaxed grains which have a finer texture, formed at the SZ. Microstructure specimen 7 (refer Fig. 11) reveals the metal flow in the onion ring layers with alternate finer and coarser grains. Microstructure specimen 8 (refer Fig. 11) is captured at the base part of the weld zone which has extremely finer grains of order 4-6μm. When moved downwards from the top of the weld zone, a refinement in grain size was observed as seen from microstructure specimen 8 (refer Fig. 11)[16].

Microstructure specimen 9 (refer Fig. 11) shows onion ring pattern which has an alternate finer and coarser grain formed on the retreating side. The presence of onion ring pattern is responsible for higher strength in the SZ. The material which undergoes deformation by FSW process produces fine grains; whereas areas near the HAZ are relatively coarser. In SZ or commonly known as nugget zone, ultra-fine grains are produced, owing to the significant plastic deformation, the generation of high temperature, and the dynamic recrystallization process[27]. The presence of oriented grains in the HAZ is accorded due to residual stress which is a consequence of FSW. The shoulder diameter determines the width of TMAZ and delineation with elongated, coarse and condensed grains is observed in TMAZ. During welding, amid the region corresponding to the placement of pin, a zone called the “stir zone” is developed, due to the material flow to and from parent specimens (AA2219-T87 and AA2014-T4 aluminium alloys). This has been illustrated by the microstructure specimen 6 and 8 of Fig.11. The said SZ, where the pin has penetrated and stirred, undergoes a maximum deformation and the presence offine grain recrystallized material distinguishes the SZ from the other regions. Analyses using SEM,EDAX and XRD are performed at the interface of the weld, where the probability of formation of intermetallic materials is high (see sections 3.6 and 3.7).

3.5 Micro-hardness characterization

Hardness mapping was done for PS1 16 weldment at a distance of 1mm, 2.5 mm, 4 mm from the top of the weld surface, as illustrated in Fig 12, and the total thickness is machined to be 5mm. Heat input has a remarkable effect on the hardness values especially in heat treatable aluminum alloys. Higher the heat input, lower is the hardness because of the dissolution of the precipitate in stir zone and due to higher cooling time resulting in the formation of coarser grains. The top region of weld experiences lower hardness because of higher heat input between the shoulder and workpiece resulting in formation of higher intermetallic layers; whereas fine grains are obtained at the center as well as bottom of weld because of adequate stirring action provided by the threaded pin and this phenomenon has the hardness in the said regions. The hardness of AA2014 side is improved significantly in the weld region due to formation of copper particles which are dispersed uniformly without dissolving or agglomerating.

From the hardness graph (refer Fig. 12), it is observed that the hardness decreases in the advancing side due to the dissolution of precipitates. This is because, the advancing side experiences maximum heat due to cyclic contact of tool and workpiece. This creates a pressure difference permitting material to flow easily from the high pressure to the low-pressure side. As the slip rate is more in advancing side, higher heat generation is observed in the said region. This excess heat coarsened and dissolved precipitates in the stir zone resulting in a decrease in the hardness; as a result of which failure occurs in the advancing side. On the retreating AA 2014 side, the presence of dispersed undissolved finer particles and formation of

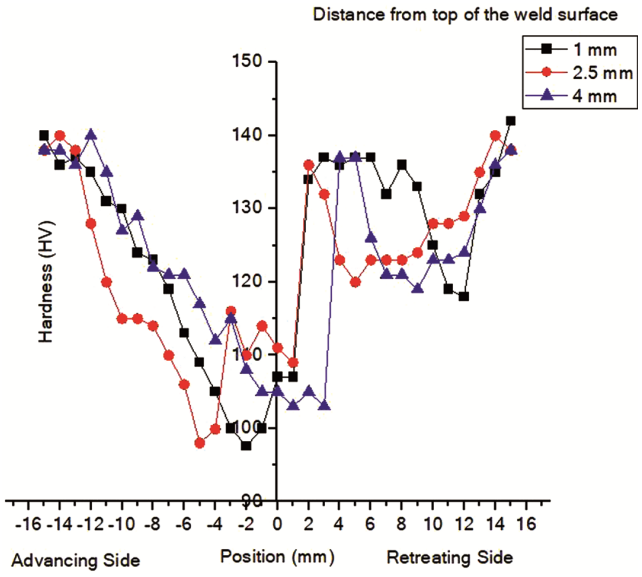

Fig. 12 — Hardness mapping of confirmation run welded sample.

intermetallic layers resulted in an increased hardness compared to base materials. The formation of intermetallic layer and dispersion of particle are clearly explained in the fractography (see section 3.6).

3.6 Fractography and EDS mapping

Once tensile testing is done, the failure region or fracture surface is subjected to fractography to determine the mode of fracture. The SEM images of the Pareto solution 1 with higher UTS and elongation were captured and analysed.

From Fig. 13 (a), dimples filled with dispersion of second phase particles are observed avoiding agglomeration or precipitate coarsening. The presence of dimples suggests ductile failure mode. The primary reason for the ductile failure is due to the formation of minute voids at the regions closer to the second phase; where as the secondary reason is observed to be the presence of inclusions, which further propagates as crack. Coalescence of these cracks occurs by the elongation of the voids which results in elongated dimples. Upon closer examination at a working distance of 17.03mm, Fig. 13(b) shows the existence of cracked second-phase particles inside the dimples, which have coarsened due to the effect of heat, suggesting a brittle like behaviour. These observations signify a mixed ductile-brittle failure in the specimen

To determine the composition of the second-phase particles, an Elemental X-ray Spectrum mapping is conducted within the precipitate region (illustrated in Figure 13(b) as point 1 and 2) using EDS. To identify the amount of copper content present in the intermetallic, point mapping of base point 1 and 2 is presented in Table 14. Further Plot of the elements present in the fractured PS1 sample at base point 1 and 2 are shown in Fig 14(a) and (b).

Point 1 and 2 marked in Fig. 13(b) exhibited around 85% of copper dispersed intermetallic particles (see Table 13). If the precipitate is coarsened, then there is a high probability of void formation and if the precipitate dissolves, then softening of weld nugget can be observed. The dispersion of copper particle over the weld zone increases the bonding strength and restricts the void formation or the crack initiation. Fig 15 (a) shows the EDS mapping of all elements in point 1 and Fig 15 (b)

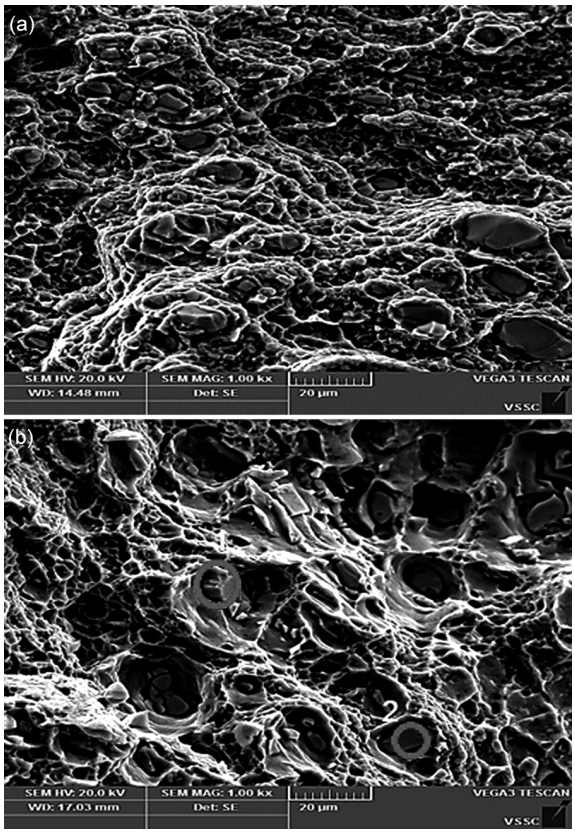

Fig 13 — SEM images of Pareto solution 1 after Fracture (a) at WD of 14.48mm, and (b)WD of 17.03mm

Table 14 — SEM-EDS Weight Percentage

	O-K	Al-K	Cu-K
Point 1	0.38	13.01	86.16
Point 2	0.24	11.51	87.99

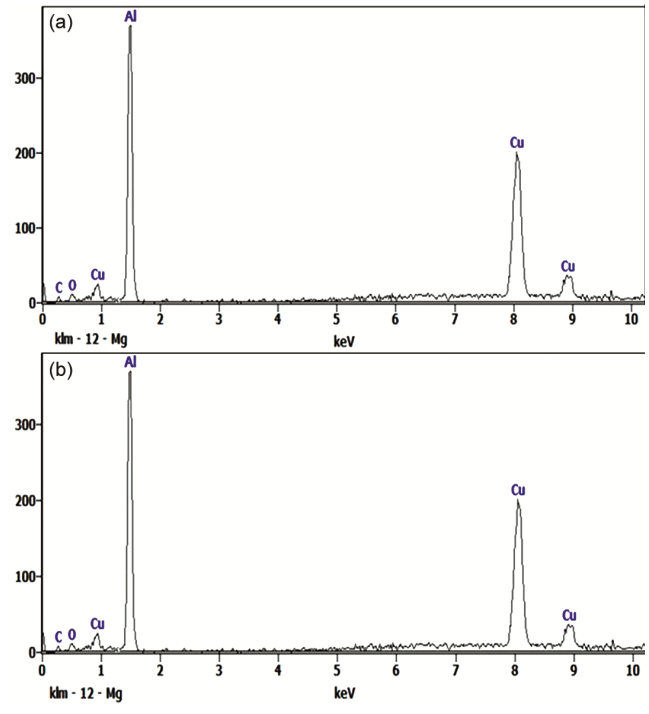

Fig 14 — Plot of the elements present in the fractured Pareto sample 1 at (a) point 1, & (b) point 2.

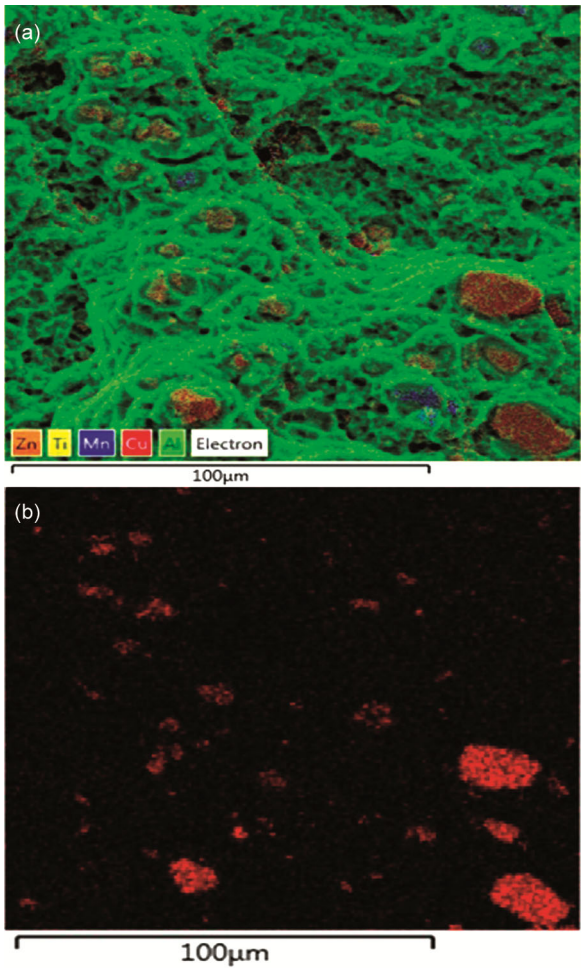

Fig. 15 — EDS mapping of point 1 (a) elemental mapping, & (b) Al-Cu mapping.

shows the aluminium and copper intermetallic at point 1. From, Fig 15(a) and (b) a uniform dispersion of Cu in Al matrix which is assumed to be the main factor controlling the strength can be observed. The dispersed Cu particles were neither agglomerated nor dissolved; instead under the optimized parameter setup, a nominal heat was generated resulting in the uniform dispersion of the Cu particles throughout the weld as shown in Fig. 15 (b).

3.73.7 XRD Analysis

Different phases present in the weld region can be known from the XRD analysis. The confirmation Pareto sample 1 which exhibits better weld strength is considered for this analysis. Al_2Cu intermetallic phases is detected in XRD analysis which is dispersed throughout the weld region and supports the strengthening of the weld zone. This strengthening particle increases the strength of AA2219 and

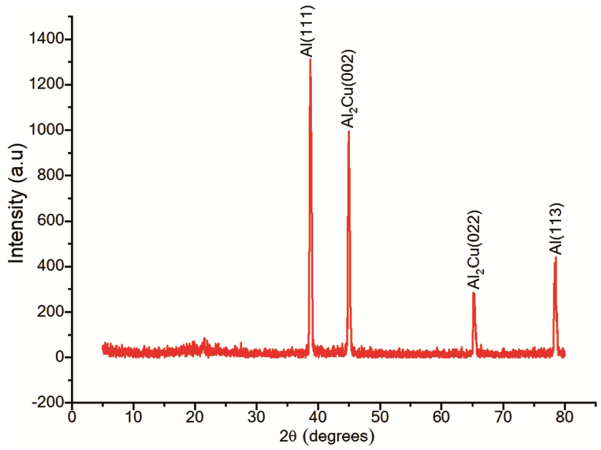

Fig. 16 — X-Ray Diffraction Pattern of the welded Sample.

AA2014 weld joints drastically. Along with this, there are other phases found as mentioned in Fig 16 which further supports the increased joint efficiency.

4 Conclusions

FSW is a distortion process that results in layer by layer material addition pushed back during every rotation of tool[9] . Macrostructural analysis revealed that greater levels of rotational speed as well as lower levels of traverse speed leads to the formation of flash and nugget collapse. On the other hand, increment in traverse speed accompanied by decrement in the rotational speed leads to the formation of worm hole defect due to lesser heat input[28].Thus parametric optimization is essential to ensure more satisfactory joint efficiency. The Pareto optimized sample revealed that the rotational speed and tilt angle have the highest impact on tensile, yield and elongation and tool profile has the least impact. Highest tensile strength and superior percentage elongation is attained by the parameter setting-1400rpm Rotational Speed, 300mm/min Welding Speed, Tapered Threaded Pin tool profile and 3º Tilt Angle; however the parameter setting 800rpm Rotational Speed, 300mm/min Welding Speed, Tapered Threaded Pin tool and 3º Tilt Angle resulted in better yield strength compared to the former parameter setting. On the other hand, multi-response optimization using AUGMECON revealed that the rotation speed and tool tilt angle determined the trade-off between the UTS, YS and elongation. The microstructural analysis revealed that the grain in the lower half was finer than that of the upper half[3]. It also revealed that the finer grains found at nugget zone resulted in strong bonds among the alloys, AA2014 and AA2219. The micro-hardness analysis showed that the hardness of the

weld was closer to parent material in retreating side and weaker hardness was observed in advancing side where the failure occurs. The fractography showed a mixed ductile-brittle failure mode. The dispersion of copper particles, which is generated during welding, throughout the weld region increased the weld strength as the copper particles act as binders and resist void formation. Morphology of a planar disk-like surface with GP zone, rich in copper, is discovered[29]. The said optimized parameter setting avoids agglomeration leading to coarser precipitate which increases the void formation on strain and increases the dissolution of precipitate which in turn softens the weld nugget. By EDS analysis, it was observed that about 85% of particles dispersed at crater region were copper and this result was validated by XRD analysis.

Acknowledgement

The authors gratefully acknowledges the Vikram Sarabhai Space Centre (VSSC - ISRO), Trivandrum for funding the research work with the project (ISRO/RES/3/683/15-16 dt.07.08.2015), Friction Stir Welding of Aluminum Alloys for aerospace applications under ISRO-RESPOND project scheme and providing the necessary facilities for the research work.

References

1 Srivatsan TS, Vasudevan S, Park L *MaterSci Eng A*, (466) (2007) 235.
2 Srinivasan PB, Arora KS, Dietzel W, J Alloys Comp, 492 (2010) 631
3 Chen Y, Liu H, Feng *J Materials Science and Engineering A*420 (2006)215.
4 Mishra RS, Ma ZY,*Mater Sci Eng R Rep*, 50(2005)1.
5 Threadgill PL, Leonard AJ, Shercliff HR, *Int Mater Rev*, (2013) 6608:.
6 Debroy T, Bhadeshia HKDH, Debroy T, *Sci Technol Weld Join,* (2000) 1718
7 Arora KS, Pandey S, Schaper M, Kumar R, *J Mater Sci Technol*, 26 (2010) 747.
8 Muthukumaran S, Mukherjee SK,*Sci Technol Weld Joi,* 11 (2006) 337
9 Krishnan KN, *Mater Sci Engi* A,327 (2002)246.
10 Rajendran C, Srinivasan K, Balasubramanian V, *Adv Materials Proc Technol*, 4(2018) 100.
11 Zhao YH, Lin SB, Wu L, Qu FX, *Mater Letters*, 59 (2005) 2948.
12 Journal I, Mechanics A (2017) 12:135–146
13 Devaraju A, *Mater TodayProc*,(2017)3722.
14 Rajendra Prasad S, Kumar A, Sridhar Reddy C, *Mater Today: Proc*, (4) 10207.
15 Chen S, Zhou Y, Xue J, (2017) J Mater Eng Perform 26 (2017) 1337.
16 Xu W, Liu J, Luan G, Dong C, *Mater Design*, 30 (2009) 3460.
17 Koilraj M, Sundareswaran V, Vijayan S, Rao SRK, *Proc Eng,* 42 (2012) 1.
18 Kang J, Feng ZC, Frankel GS, *Phys Metal Mater Sci,* 47(2016) 4553.
19 Kang J, Feng ZC, Li JC, *Phys Metal Mater Sci*, 47 (2016) 4566.
20 Malarvizhi S, Balasubramanian V *Mater Design*, 32 (2011) 1205.
21 Zhang C, Huang G, Cao Y, *J Mater Eng and Performance*, (2017)
22 Marthaler DE,*Numerical Methods for Metamaterial Design* 127(2013)31.
23 Zhao Z, Liang H, Zhao, Y, & Yan, K, *J MaterEng Perform*, 27(2018) 1777.
24 Ju-Long D,*grey systems Systems*, 1(1982)288.
25 Khodabakhshi F, *Mater Sci Eng A*, 666 (2016) 225.
26 M A Sutton, B Yang, A P Reynolds, R Taylor,*Mater Sci Eng A*, 323(2002)160.
27 Rafiei R, Moghaddam AO,*IntJ Adv Manuf Technol,* 90 (2017) 2785
28 K V Jata, S L Semiatin,*ScrMater*, 43(2000)743.
29 Malarvizhi S, Balasubramanian V J Mater Eng Perform, 20(2011) 359.
30 Kumar, K, & Singh H, Chinese *J Mech Eng*, 36(1)(2023) 1.
31 Mohan, D G, & Wu C, Ch JMech Eng, 34(2021)1.
32 Horton, K R (Doctoral dissertation, The University of Alabama) (2011).
33 Narayana Murty, S V S, & Sharma S C, J Indian Inst Sci, 102 (1) (2022) 513.
34 Satyanarayana, M V N V, Bathula S, & Kumar A, *Mater Lett*, 305 (2021) 130757.
35 Wang, G, Zhao Y, & Hao Y,*J MaterSci & Technol*, 34 (1) (2018) 73.
36 Mazaheri H, Aval H J, & Jamaati, R, *Mater Sci Eng A*, 826(2021) 141958.
37 Quarto M, BocchiS, DUrsoG, & Giardini C, *J Eng Manuf*, (2022).
38 Keerthipalli T, Aepuru R, & BiswasA, J EngManuf, 237 (6) (2023) 833